

Helical particle manipulation based on power-exponent-phase Acoustic vortices generated by a sector transducer array

Qingdong Wang(王青东), Yantao Hu(胡彦涛), Shengli Wang(王胜利), and Hongyu Li(李洪宇)
Citation: Chin. Phys. B, 2023, 32 (**6**): 064304. DOI: 10.1088/1674-1056/acc800
Journal homepage: http://cpb.iphy.ac.cn; http://iopscience.iop.org/cpb

What follows is a list of articles you may be interested in

Controlling acoustic orbital angular momentum with artificial structures: From physics to application

Wei Wang(王未), Jingjing Liu(刘京京), Bin Liang (梁彬), and Jianchun Cheng(程建春)
Chin. Phys. B, 2022, 31 (**9**): 094302. DOI: 10.1088/1674-1056/ac7868

Acoustic radiation force on a rigid cylinder near rigid corner boundaries exerted by a Gaussian beam field

Qin Chang(常钦), Yuchen Zang(臧雨宸), Weijun Lin(林伟军), Chang Su(苏畅), and Pengfei Wu(吴鹏飞)
Chin. Phys. B, 2022, 31 (**4**): 044302. DOI: 10.1088/1674-1056/ac2d1f

Measuring orbital angular momentum of acoustic vortices based on Fraunhofer's diffraction

Chao-Fan Gong(龚超凡), Jing-Jing Li(李晶晶), Kai Guo(郭凯), Hong-Ping Zhou(周红平)†, and Zhong-Yi Guo(郭忠义)‡
Chin. Phys. B, 2020, 29 (**10**): 104301. DOI: 10.1088/1674-1056/ab9c11

Random phase screen influence of the inhomogeneous tissue layer on the generation of acoustic vortices

Zhiyao Ma(马致遥), Jun Ma(马骏), Dong Zhang(章东), Juan Tu(屠娟)
Chin. Phys. B, 2018, 27 (**3**): 034301. DOI: 10.1088/1674-1056/27/3/034301

Multiple off-axis acoustic vortices generated by dual coaxial vortex beams

Wen Li(李雯), Si-Jie Dai(戴思捷), Qing-Yu Ma(马青玉), Ge-Pu Guo(郭各朴), He-Ping Ding(丁鹤平)
Chin. Phys. B, 2018, 27 (**2**): 024301. DOI: 10.1088/1674-1056/27/2/024301

Helical particle manipulation based on power-exponent-phase acoustic vortices generated by a sector transducer array

Qingdong Wang(王青东)[1,†], Yantao Hu(胡彦涛)[2], Shengli Wang(王胜利)[1], and Hongyu Li(李洪宇)[1]

[1] *College of Ocean Science and Engineering, Shandong University of Science and Technology, Qingdao* 266590, *China*
[2] *Department of Modern Architecture, Linyi Vocational College, Linyi* 276017, *China*

(Received 9 January 2023; revised manuscript received 6 March 2023; accepted manuscript online 28 March 2023)

The characteristics of traditional acoustic vortices (AVs) were verified by the cross-sectional axisymmetric pressure distributions with perfect phase spirals around the center pressure null. In order to generate a non-axisymmetric pressure distribution, the concept of power-exponent-phase was first introduced into the formation of AV beams, named "power-exponent-phase acoustic vortices (PAVs)" in this paper. Based on a ring-array of sector transducers, the helical distribution of the low-pressure valley in cross-sections of PAVs, which enables particles to move from a distant position to the center low-potential well along a certain spiral passageway, was proved theoretically. The particle manipulation behavior for PAVs with a power order of 2 is numerically modeled and experimentally confirmed. The results show that PAVs with a non-axisymmetric spiral pressure distribution can be used to realize the directional transport of particles in an enlarged scope, suggesting prospective application potential in biomedical engineering.

Keywords: acoustic vortices, power-exponent-phase, spiral potential well, sector transducer array, particle manipulation

PACS: 43.72.+q, 43.38.Hz **DOI:** 10.1088/1674-1056/acc800

1. Introduction

The optical vortex is a helical beam[1,2] with broad application prospects in micro-manipulation,[3,4] information communication[5,6] and micro- and nanomachining.[7,8] During the axial propagation of light waves, the phase change around the center determines the handedness and rotation speed of the phase spiral. The orbital angular momentum (OAM) carried by the optical vortex can be used to drive small objects in a rotational manner.[9] The intensity in cross section exhibits an axisymmetric circular or high-order Gaussian distribution.

Inspired by the optical vortex, numerous methods of generating vortices have been actively explored in the fields of electronics[10,11] and acoustics.[12,13] The concept of the acoustic vortex (AV) was first proposed by Broadbent in 1979,[14] and the stability and boundary conditions at infinity were introduced. In 1998, Hefner[15] used a transducer composed of a brass ring and PVDF to generate an AV beam. The annular transducer had a helical radiation surface at the operating frequency of 300 kHz. Additionally, common features of OAM transfer and object spinning were also demonstrated. The studies discovered that small objects, such as particles, cells, and organisms, could be moved and rotated by AVs in three-dimensional space. Therefore, the search for AV field optimization is of great application significance for non-contact object manipulation.

The optoacoustic generation of a helicoidal ultrasonic beam was demonstrated by Gspan.[16] It was produced by illuminating a specially structured absorbing surface in a water tank with pulsed laser light. The absorbing surface had a profile with a screw dislocation, similar to the transverse cross-sectional surface of a helix. A phase-coded approach was proposed by Yang and Ma to construct a controllable AV beam using circumferentially distributed point sources.[17] Then, based on the phase-coded approach, the influences of parameters on AVs were discussed in both theory and experiment.[18–20] A scheme based on multi-arm coiling slits was proposed to generate stable AVs in a broadband, which was able to spiral acoustic waves spatially and twist AVs with an invariant topological charge for a long propagation distance.[21] Compared with the traditional methods using complex electronic systems, this study provided an effective and convenient solution for AV construction.

The AVs generated by the above mentioned methods have the typical characteristics of a phase spiral of wave fronts and the pressure null at the vortex center. The most remarkable feature of AVs was proved by theoretical derivations and experimental measurements. The capability for particle trapping and manipulation was proved by Courtney using a circular chamber structured by a 16-element transducer array.[22] By changing the phase of the driving sinusoidal signals, microparticles were moved by the Bessel-function AV field. By increasing the transducer number to 64, Hong *et al.*[23] moved and rotated microparticles of various materials, such as polystyrene, flour, and silicon, only in two dimensions.

However, the previous experimental results demonstrated that most of particles were bounded in the pressure valley re-

[†]Corresponding author. E-mail: wangqingdong@sdust.edu.cn
© 2023 Chinese Physical Society and IOP Publishing Ltd

gion between two circles of pressure peak, and could not move to the vortex center.[24] This result is due to the annular pressure distribution produced by the topological charge of integer orders. Despite that fractional AVs could be generated by a circular array of sources using multiple ramps of phase-delay to break the symmetry pressure distribution,[25] and the resultant AVs showed a fascinating variety of shapes such as points, dashes, triangles and squares, the capture range could not be expanded easily by non-integer orders.

In the current study, the concept of power-exponent-phase is introduced into AVs for the first time, and non-axisymmetrical vortex fields with a strengthened acoustic gradient force are generated by a sector transducer array.[26] A three-dimensional (3D) distribution of the helical potential well is observed in the fields of power-exponent-phase AVs (PAVs), which suggests the unique capability of moving objects from a distant position to the center potential well along a certain spiral passageway. The experimental and simulation results indicate that PAVs can be applied to expand the trapping range, exhibiting good application potential for directional manipulation in biomedical engineering.

2. Principle and method

An N-element sector transducer array with the radius a is adopted to generate AV beams, as shown in Fig. 1. In the source plane, N sector planar piston transducers are distributed uniformly to form a complete circle. The spatial angle of each sector source is $\Delta\varphi = 2\pi/N$. The initial phase function of the n-th sector is expressed by $\phi_n = 2\pi l\left[(n-1)/N\right]^m$, where l and m are the topological charge and the power order of spiral phase,[27] respectively. Assuming the surface vibration is perpendicular to the source plane at the same strength, the particle velocity on each point on the nth sector transducer can be described by $A = A_0\exp\left[\mathrm{j}(\omega t - \phi_n)\right]$, where A is the particle velocity amplitude and ω is the angular frequency.

By dividing the sector surface into infinite infinitesimal portions, each vibration element can be treated as a unit source to create a spherical radiation in free space. Thus, the acoustic pressure at the observation point produced by the nth sector source can be calculated by

$$\mathrm{d}p_n(r,\phi,z) = \frac{\mathrm{j}k\rho_0 c_0}{2\pi R_n} A_0\,\mathrm{d}S_n \exp\left[\mathrm{j}(\omega t_n - kR_n - \varphi_n)\right], \quad (1)$$

where $\mathrm{d}S_n = r_n\,\mathrm{d}r_n\,\mathrm{d}\varphi_n$ is the area of the unit source in cylindrical coordinates,

$$R_n = \sqrt{\left[r\cos\phi - r_n\cos\phi_n\right]^2 + \left[r\sin\phi - r_n\sin\phi_n\right]^2 + z^2}$$

is the transmission distance from source $(r_n, \varphi_n, 0)$ to observation position (r,φ,z) and $t_n = R_n/c_0$ is the corresponding transmission time, ρ_0 and c_0 are the density and acoustic speed of the medium, and $k = \omega/c_0$ is the wave number. The acoustic pressure at the observation point generated by the sector transducer array can be derived as

$$p(r,\varphi,z) = \sum_{n=1}^{N}\frac{\mathrm{j}k\rho_0 c_0}{2\pi}A_0\int_0^a\int_{\varphi_n}^{\varphi_n+\Delta\varphi}\frac{\mathrm{e}^{\mathrm{j}(\omega t_n - kR_n - \phi_n)}}{R_n}r_n\,\mathrm{d}r_n\,\mathrm{d}\varphi_n. \quad (2)$$

The relationship between the acoustic pressure and the particle velocity can be described by the motion equation $\rho\frac{\partial v}{\partial t} = -\nabla p$, where $\nabla = \hat{r}\frac{\partial}{\partial r} + \frac{1}{r}\hat{\varphi}\frac{\partial}{\partial\varphi} + \hat{z}\frac{\partial}{\partial z}$ is the gradient operator in cylindrical coordinates, and $\hat{r}$, $\hat{\varphi}$, and $\hat{z}$ are the unit vectors along the respective directions. Then, the particle velocity $\boldsymbol{v}_\perp$ in the transverse plane can be calculated from $\nabla_\perp p/(\mathrm{i}\omega\rho)$, where $\nabla_\perp = \nabla - \hat{z}\partial/\partial z$. Hence, the transverse particle velocity can be calculated as $\boldsymbol{v}_\perp = \left(\hat{r}\frac{\partial p}{\partial r} + \hat{\varphi}\frac{1}{r}\frac{\partial p}{\partial\varphi}\right)/(\mathrm{i}\omega\rho_0)$. In object manipulation, the capability of particle trapping and rotating is often described by the exerted acoustic gradient force (AGF)[28] as

$$F_\perp = -\nabla U_\perp = -\pi a_\mathrm{p}^3\left\{\left[1 - \frac{c^2\rho}{c_\mathrm{p}^2\rho_\mathrm{p}}\right]\frac{\nabla|p|^2}{3\rho c^2} - \left[\frac{2(\rho_\mathrm{p}-\rho)}{2\rho_\mathrm{p}+\rho}\right]\frac{\rho\nabla|\boldsymbol{v}_\perp|^2}{2}\right\}, \quad (3)$$

where $U_\perp$ is the Gor'kov potential[28] in the transverse plane, and a_p, ρ_p, and c_p are the radius, density, and acoustic speed of the particle, respectively.

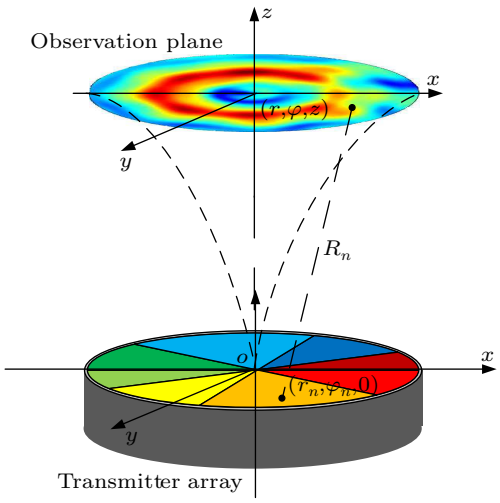


Fig. 1. Sketch diagram of constructing PAV beams using a sector transducer array.

3. Numerical studies

Numerical simulations are conducted using MATLAB programming. The experimental sector transducer array with $a = 40$ mm and $N = 8$ is used as the source with different initial phases at the working frequency of $f = 500$ kHz, where $c = 1500$ m/s and $\rho = 1000$ kg/m^3. As shown in Fig. 2(a), the cross-sectional pressure distribution of the AV with $m = 1$

is axisymmetric and the area of the central potential well increases with the increase of topological charge. Meanwhile, the vortex radius increases gradually with the increase of the axial distance, while the phase singularity is always on the beam axis. Although the center potential well of AVs can be used to trap objects, the annular high pressure still hinders the object motion to the vortex center from outside. Hence, objects can be patterned around the surrounding low-pressure circle as shown by the dashed line. The asymmetric pressure distribution of the PAV with $m = 1$ and $l = 1$ is presented in Fig. 2(b), which shows a spiral low-pressure region around the center. The spiral radius decreases gradually in the clockwise direction, and an approximately circular low-pressure region deviated from the field center is formed. The application of a PAV is implementation of a unique capability to move objects from a distant position to the center potential well along a certain spiral passageway.

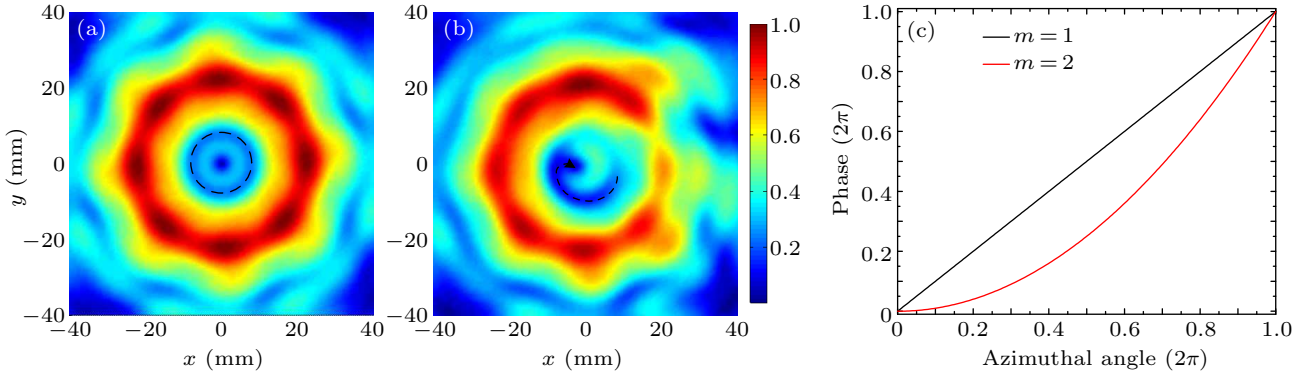


Fig. 2. Cross-sectional pressure distributions of (a) the traditional AV with $m = 1$, (b) the PAV with $m = 2$ for $l = 1$, and (c) the azimuthal angle distribution of phase at $z = 205$ mm.

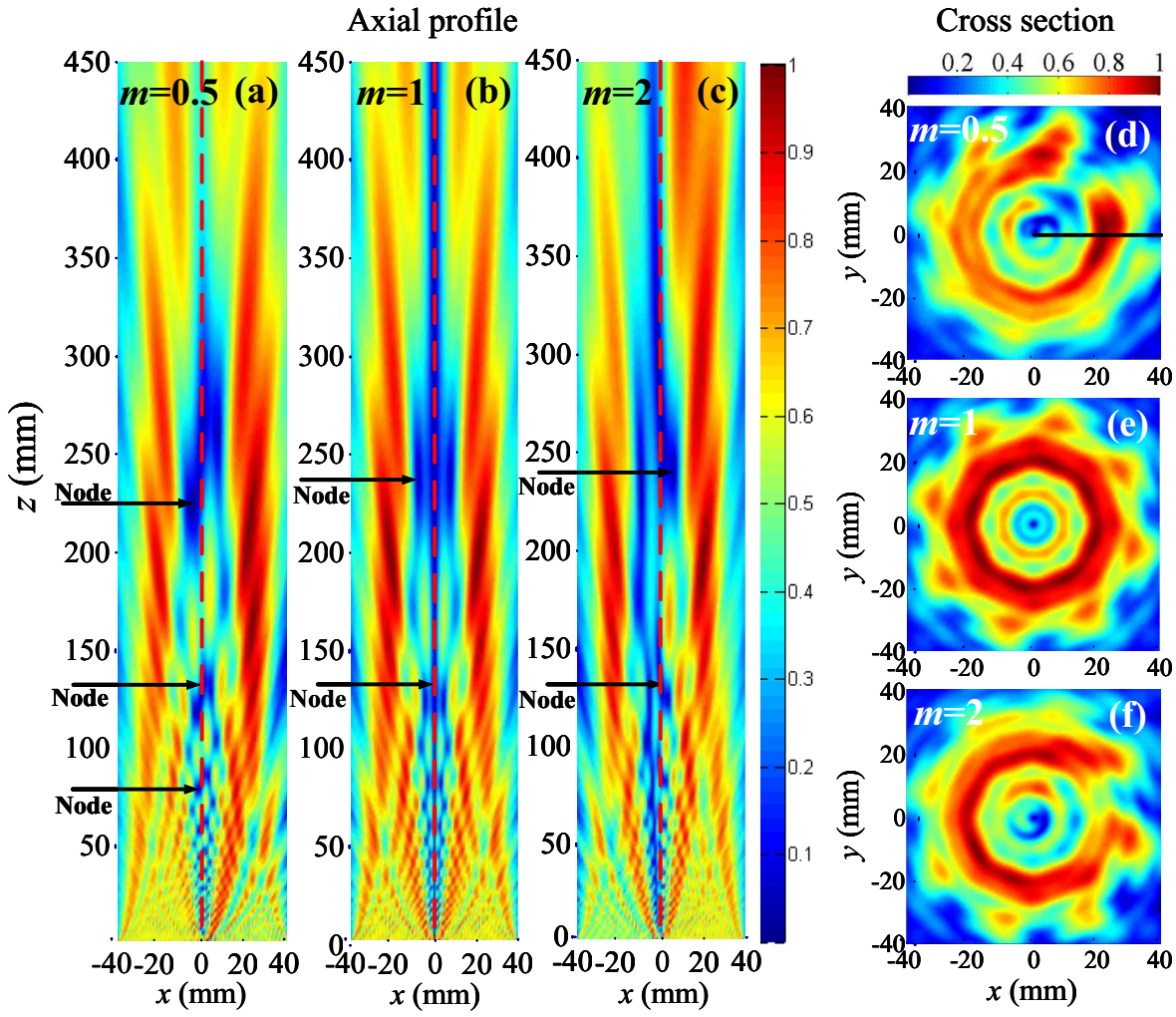


Fig. 3. Axial pressure profiles of the PAVs with m values of (a) 0.5, (b) 1, and (c) 2, and (d)–(f) the corresponding cross-sectional pressure maps at $z = 135$ mm.

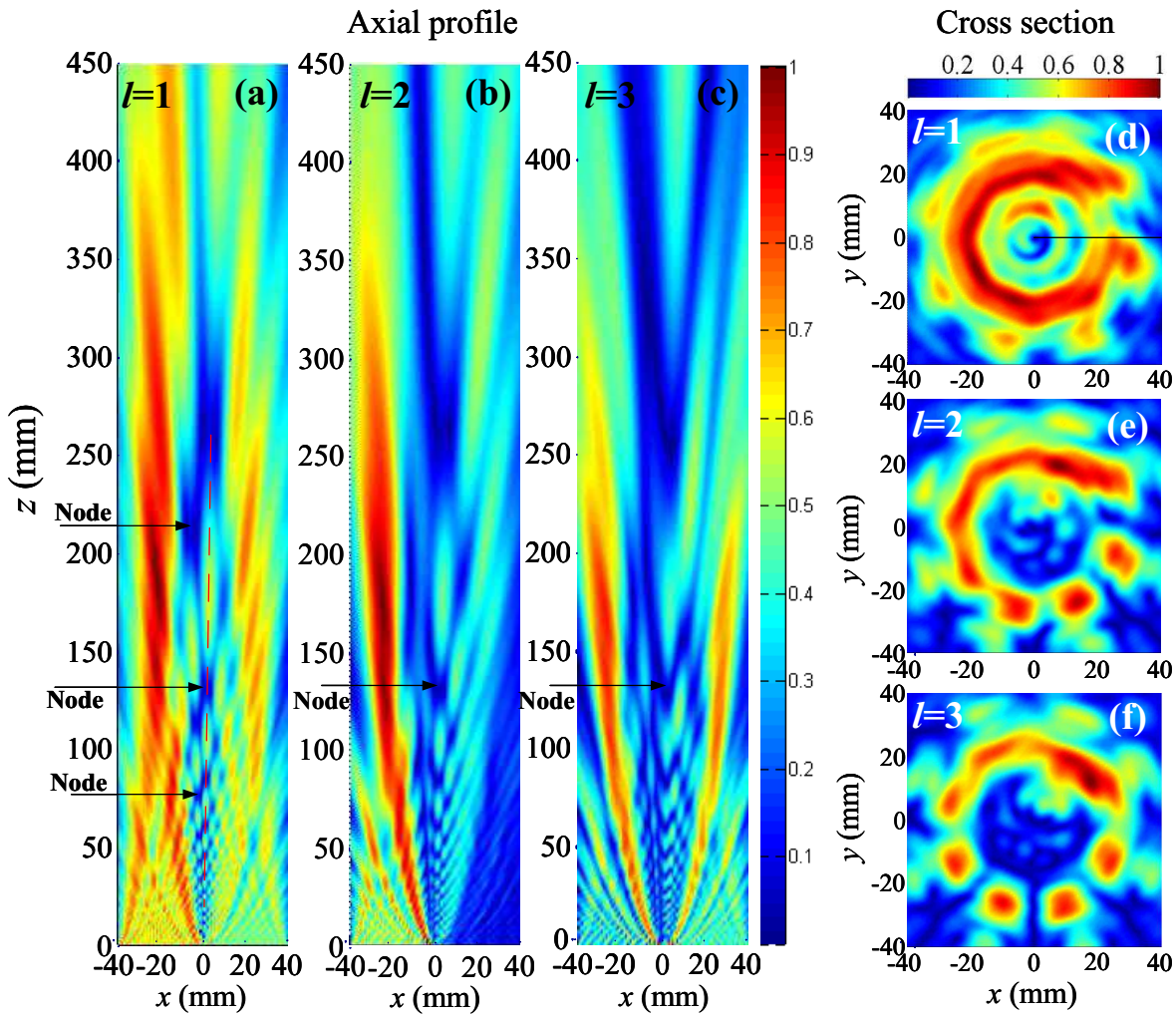


Fig. 4. Axial pressure profiles for PAVs with $m = 2$ and l values of (a) 1, (b) 2, and (c) 3, and (d)–(f) the corresponding cross-sectional pressure distributions at $z = 135$ mm.

To get a deeper understanding of the phase characteristics for PAVs, the azimuthal phase distributions for different power exponents are calculated and plotted in Fig. 2(c). When the azimuthal angle changes from 0 to 2π, the phase distribution for AV with $m = 1$ is continuous and linear, as shown by the black line. In contrast, the nonlinear phase distribution created by the PAV with $m = 2$ (red line) exhibits an increasing tendency with a rising slope for a bigger azimuthal angle, indicating a server deviation from the field center. It can be drawn that the power exponent is an important parameter affecting the field distributions of pressure and phase.

The characteristics of PAVs with different power exponents are also analyzed and the axial pressure profiles for $l = 1$ and $m = 0.5$, 1, and 2 are plotted in Fig. 3, with the red dashed lines indicating the z-axis. For $m = 0.5$, an asymmetric pressure profile can be observed in Fig. 3(a), and multiple nodes are distributed on both sides of the z-axis. The area of the potential well increases with the increase of the axial distance. The pressures on both sides of the on-axis nodes (i.e., $z = 135$ mm) are relatively higher. Just like the axial pressure profile for $m = 1$, the pressure distributions are more divergent in the near-field, while, for the symmetric distribution of the traditional AV for $m = 1$ as shown in Fig. 3(b), an axial low-pressure potential well channel is formed along the z-axis. The symmetrical regions of low-pressure valleys are formed on both sides of the vortex center. For $m = 2$, the non-axisymmetric axial pressure profile in Fig. 3(c) shows the low-pressure region deviates from the z-axis. Potential wells are also formed on both sides of the z-axis and separated by the high-pressure regions.

The cross-sectional pressure map at $z = 135$ mm for the traditional AV is also presented as a perfect symmetrical distribution with zero pressure at the vortex center, as shown in Fig. 3(e). Several low-pressure circles appearing in the cross-section can be used to capture particles on the annuli, while for $m = 0.5$ and 2, the cross-sectional pressure maps as shown in Figs. 3(d) and 3(f) present asymmetric distributions. The paraxial pressure increases or decreases gradually with the azimuthal angle, being obviously different from that of the traditional AV. In addition, the vortex center of the PAV with $m = 0.5$ is still located on the z-axis, while it deviates from the z-axis for PAV with $m = 2$.

In order to obtain the detailed characteristics of the PAV with $m = 2$, the axial and cross-sectional pressure distributions for $l = 1$, 2, and 3 are simulated as illustrated in Fig. 4. The acoustic field of the PAV with $l = 1$ is more divergent with the increase of the propagation distance, as shown in Fig. 4(a). Multiple trapping can be realized by the low-pressure nodes distributed alternately on both sides of the z axis at different axial positions. As the axial distance increases, the radial distance of the node from the propagation axis increases in a larger region. Meanwhile, with the increase of the topological charges as shown in Figs. 4(b) and 4(c), the node distribution becomes messier with a longer radial distance due to a more divergent effect. The cross-sectional pressure distributions at $z = 135$ mm corresponding to $l = 1$, 2, and 3 are shown in Figs. 4(d)–4(f). The position of the potential well deviates from the z axis. An approximate high-pressure annular is generated by the PAV of $l = 1$ with an anticlockwise spiral region formed near the z axis. Thus, under the action of the carried OAM of PAVs, there is always a suitable axial position to move objects along the spiral pathway to the center potential well. Whereas, for the annular pressure distribution, it is more difficult to form a spiral distribution near the propagation axis for a higher l, therefore, the optimized topological charge of $l = 1$ should be selected for object migration by PAVs.

Also as shown in Fig. 4(a), the pressure valley on the right side of the z axis are precisely distributed on the red dashed line, whose azimuthal angle is $\theta = 0$ corresponding to the projection on the cross section as the black solid line in Fig. 4(d). The angle between the red dashed line and the z axis is $\varphi = 6.5°$. In other words, as the propagation distance increases, the distance between the pressure valley and the z axis also increases. The axial pressure distribution on the red dashed line for $\theta = 0$ is displayed in Fig. 5(a), which is generated by PAVs with $l = 1$. The pressure variations of the near-field fluctuation can also be observed clearly with the pressure peaks and valleys values at the corresponding vortex nodes and antinodes, indicating the formation of multiple traps at vortex nodes. The other curves for $\theta = \pi/6$, $\pi/3$, and $\pi/2$ have similar pressure fluctuations. The pressure peak increases with the increase of the angle, while the pressure valley keeps basically consistent. It is also worth noting that the axial distance of the potential well also decreases as the azimuthal angle increases: 130.7 mm, 128.1 mm, 125.9 mm, and 124.2 mm for $\theta = 0$, $\pi/6$, $\pi/3$, and $\pi/2$, respectively. The distribution of the potential well with respective to the angle is presented in Fig. 5(b). The axial distance is shortened by 45.7 mm when θ is varied from 0 to 2π. Thus, the axisymmetric spiral distribution of the potential well in the axial direction is a cone-shaped continuous spiral pathway in the paraxial region.

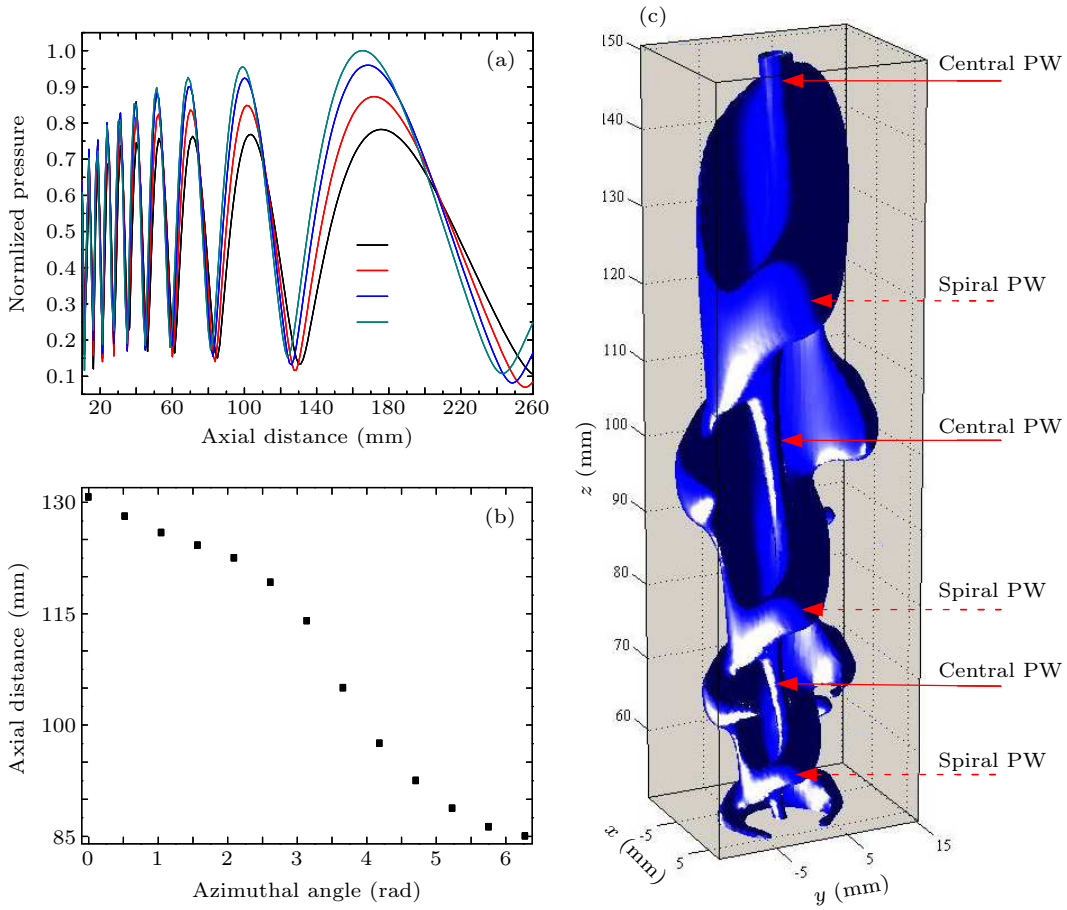


Fig. 5. (a) Axial pressure distributions along the red dashed line in Fig. 3(a), (b) axial distribution of the potential well as a function of the azimuthal angle, (c) 3D distribution of the potential well (indicated by PW) for $z = 50$ mm–150 mm.

The 3D distribution of the spiral potential well is displayed in Fig. 5(c), where the high pressures are removed to ensure the pressure inside the spiral pathway is lower than on the field sides. In order to make the continuous spiral pathway more clearly, the distributions of the potential well are numerically studied for $z = 50$ mm–150 mm. The center potential wells are indicated by "central PW" in the paraxial region. A spiral potential well passageway can be used to capture smaller objects in the finite axial region. It is also apparent that spiral potential wells with a larger spiral radius can be formed in a wider axial region, which are indicated as "spiral PW" in Fig. 5(c). As the axial distance increases, the flat shape of "spiral PW" becomes thicker. The potential well rotates around the z-axis for about two turns by increasing the axial distance from 55 mm to 115 mm, demonstrating the possibility of long-distance manipulation.

Rayleigh particles with a smaller size than the wavelength are always moved from the higher pressure region to the lower one. To verify the performance of PAVs, the cross-sectional distribution of the pressure gradient vector at $z = 205$ mm for three topological charges were simulated and are displayed in Fig. 6, with the vector directions represented by blue arrows. Small objects inside the equipotential line L1 can be driven towards the vortex center by the PAV with $l = 1$ as shown in Fig. 6(a). When these objects arrive at the equipotential line L2, some of them can be captured directly to the potential well, while the others will move towards the potential well along the spiral trajectory of the pressure valley (black curve) due to the OAM transfer. Thus, the trapping range can be expanded to the radius of the spiral region (about 20 mm). Under the action of the AV with $l = 2$ as shown in Fig. 6(b), small objects outside the equipotential line L3 move towards the beam axis, and those inside the equipotential line L4 are driven outwards, hence, resulting in the final trapping at L4. In addition, for $l = 3$ as shown in Fig. 6(c), objects can be trapped in multiple regions by the equipotential lines L5, L6, and L7 rather than the single-region accumulation. Therefore, only the PAV with $l = 1$ can be used to realize the single-region aggregation in a larger area.

In order to study the direction of object motion, distributions of the acoustic intensity for PAVs of different orders at $z = 205$ mm are plotted in Fig. 7. As indicated by arrows, the direction of each intensity vector basically points to the potential well with a small direction deflection. Although the intensity near the potential well is relatively lower, the consistent spiral direction is clearly displayed for the PAV with $l = 1$ as shown in Fig. 7(a). Hence, objects can be driven along the spiral direction clockwisely towards the potential well.[23] Therefore, an off-axis larger helical potential well can be created by the PAV with $l = 1$, while, for $l = 2$ and 3, distributions of the acoustic intensity in Figs. 7(b) and 7(c) are more complex with multiple spiral potential wells.

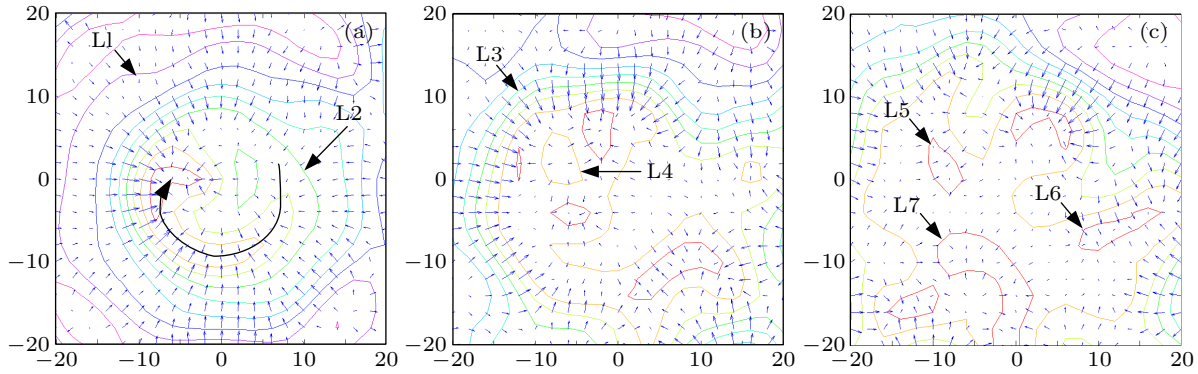


Fig. 6. Cross-sectional distributions of the pressure gradient vector at $z = 205$ mm for PAVs with l values of (a) 1, (b) 2, and (c) 3.

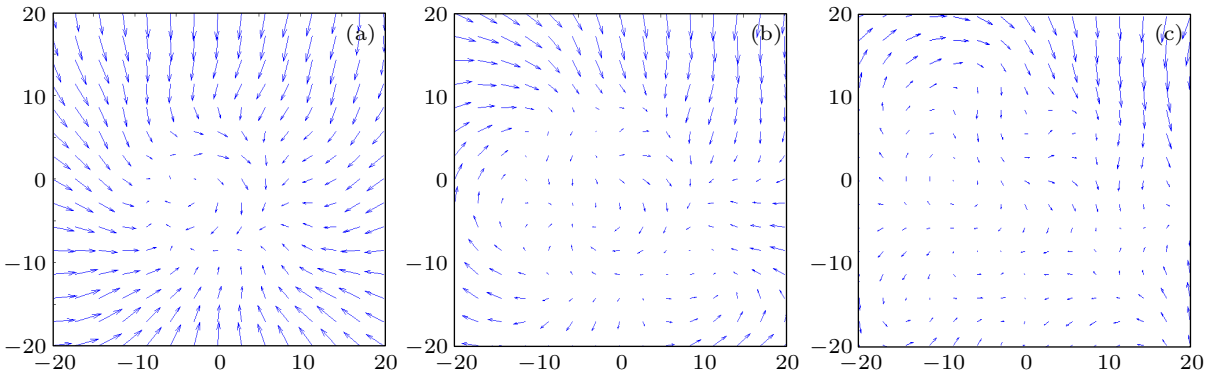


Fig. 7. Distributions of the acoustic intensity at $z = 205$ mm for PAVs with l values of (a) 1, (b) 2, and (c) 3.

Assuming the objects to be trapped are spherical polyethylene particles with $\rho_p = 918$ kg/m^3, $c_p = 1900$ m/s, and $a_p = 1.5$ mm, cross-sectional distributions of the radial AGF for the traditional AV with $l = 1$ and $m = 1$ and PAVs with $m = 2$ and $l = 1$, 2, and 3 at $z = 205$ mm are simulated as shown in Fig. 8. The positive and negative values of the AGF represent the rightward and leftward directions for particle trapping. For example, the forces exerted on the particle at $x = 0$ are pointing to the on-axis vortex center for the traditional AV, while, at $x = 4.6$ mm, the forces are leftward and rightward, resulting in the pulling effects on both sides. The vortex centers of PAVs with $m = 2$ deviate obviously from the z-axis, and the AGF direction at $x = 0$ mm is leftward. In contrast, the AGF distributions of PAVs are no longer centrosymmetric. Obvious AGF fluctuations are displayed in the radial direction with positive and negative values, further demonstrating that the AGF of PAVs cannot move particles radially in a large range.

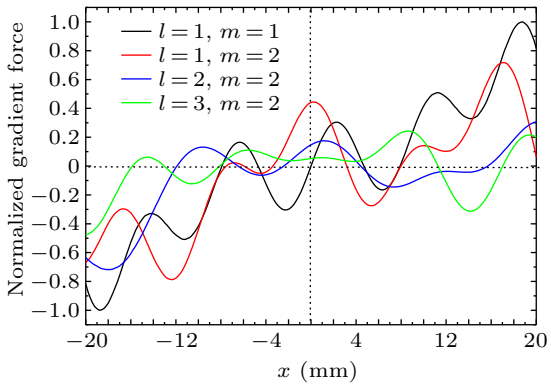


Fig. 8. Normalized radial AGF distributions of the traditional AV and PAVs.

4. Experimental studies

An 8-element sector transducer array with the radius of 40 mm at the center frequency of 500 kHz was employed for measurements. The initial phase of each transducer element increases clockwise according to $m = 2$ and $l = 1$. The axial pressure distribution scanned by a needle hydrophone shown in Fig. 9(a) for $z = 100$ mm to 260 mm is non-axisymmetric. The acoustic pressure of the left main lobe is obviously bigger than that of the right one, which is quite different from the traditional AV. Multiple pressure valleys are formed on both sides of the beam axis, and the area of the valley region increases gradually with the axial distance. The experimental valley locations are somewhat different from those of the simulation results, which might be produced by an inconsistent angle in the axial profile. Each angle corresponds to different axial distances of the spiral well in the PAVs. For example, the simulated position of the pressure valley is at $z = 130$ mm, while the experimental distance is at $z = 128$ mm.

A crescent-shaped high-pressure region is formed at $z = 205$ mm, and the corresponding cross-sectional pressure map is shown in Fig. 9(b). Being consistent with the simulation result, an approximate spiral region of pressure valley is presented near the z axis with a poor continuity, due to the limited source number. The phase distribution in Fig. 9(c) agrees well with the quadratic power function with respect to the angle. The experimental phase singularity deviates from the z axis by the inherent characteristics of the PAV.

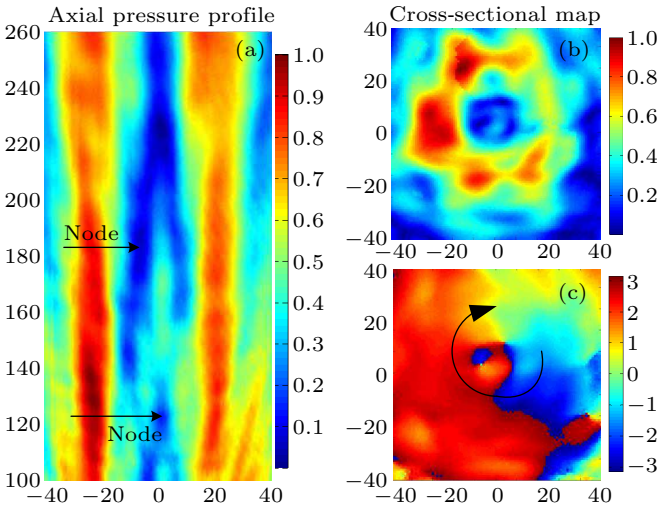


Fig. 9. (a) Experimental axial pressure profile and cross-sectional maps of (b) pressure and (c) phase for $l = 1$ and $m = 2$ at $z = 205$ mm.

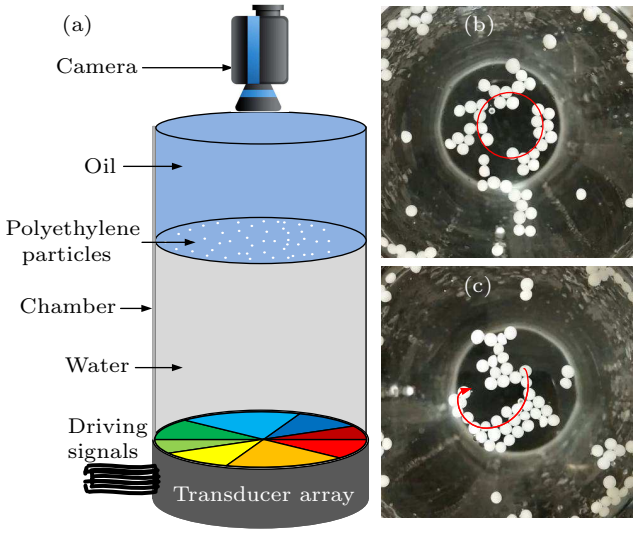


Fig. 10. (a) Model diagram of the experimental system for particle manipulation, Pictures of particle capture using the (b) traditional AV and (c) PAV with $l = 1$.

The system diagram of particle manipulation is shown in Fig. 10(a). Polyethylene particles with average diameter of nearly 1.0 mm were located at the interface between water and oil, and the pictures of particle trapping were recorded by the camera. To illustrate the advantages of PAVs, experimental results of radial trapping by the traditional AV at $z = 205$ mm is presented in Fig. 10(b) for comparison. The conclusion is

verified by the experimental annular trapping of particles (red circle). A novel experimental result for the PAV is shown in Fig. 10(c). Particles are distributed along the spiral trajectory (red arrow), being consistent with the simulation in Fig. 6(a). The clockwise rotation of the spiral matches well with the direction of the acoustic radiation torque of the PAV. Most particles in the simulation are imprisoned in the spiral pressure valley region, rather than the field center, whereas, the particle distributions in Fig. 10 are not in a strict circle or spiral. The obvious differences might be introduced by experimental factors, such as the relative larger size of particles, the electrostatic attraction between particles, the inconsistency of transducers, and so on. However, the deficiencies mentioned above can be improved by the appropriate selection of particles and the design of circuits and transducers.

5. Discussion

Although the principles of generating power-exponent-phase optic and acoustic vortices are similar in theory, broader application prospects are achieved by PAVs due to the larger size, greater AGF, longer penetration depth, and non-selection of manipulation objects, exhibiting improved manipulation capability for biomedical practice. Benefiting from the capability of breaking the annular high-pressure barrier of the traditional AVs, PAVs can be applied to trap particles from an expanded radial distance to the vortex center along a spiral low-pressure passageway, realizing directional transportation without additional field regulation.

For PAVs generated by the sector transducer array around the beam axis with acoustic pressure obviously higher than that near the wall of a big water tank (500 mm $\times$ 500 mm $\times$ 600 mm), the acoustic reflection by the boundary can be neglected in numerical studies. The axial and cross-sectional distributions of pressure and phase detected by the hydrophone in experiments are in good agreement with those in simulations. However, for the particle manipulation experiment using the cylindrical water chamber, the waveguide influence of the wall is obvious in the current study. Thus, under the action of the wall-reflected acoustic field, the pressure distribution of the PAV is varied by the composite field, resulting in particle accumulation along the spiral trajectory and particle repulsion to the chamber wall. Therefore, the boundary problem of the chamber wall should definitely be considered as an important issue in future research.

As is well known, the AGF in terms of magnitude and direction is determined by the shape and size of particles. Theoretically, when the particle diameter reaches the wavelength level, acoustic waves will be refracted and reflected significantly, resulting in an obvious influence on field distribution and particle manipulation. Thus, the particles used in the current study are not the perfect Rayleigh ones because their diameters are similar to the wavelength. However, the experimental particle diameter (1 mm) of about $1/3$ of the wavelength equals approximately the width of the potential well. Therefore, particles can be arranged individually in the potential well to observe the spiral passageway accurately.

6. Conclusion

Based on the power-exponent-phase principle, theoretical and experimental investigations on PAVs are conducted by applying a phase-coded approach using a sector transducer array. The PAV is proved to have a non-axisymmetrical exponential distribution with respect to the azimuthal angle and construct a spiral low-pressure potential well with a larger trapping range around the z-axis. An approximately circular pressure valley is formed with the vortex center deviated from the z-axis. Under the action of the OAM transfer, PAVs can be applied to move particles from the high-pressure region to the spiral potential well. The spiral potential well is alternately arranged around the z-axis, with the radial size increasing with the increase of axial distance, forming the low-pressure potential well along a spiral passageway. Experimental distributions of pressure and phase and arrangements of particles agree well with simulations. The favorable results demonstrate the feasibility of directional manipulation along a spiral low-pressure passageway in three dimensions in an enlarged area and suggest the application potential of PAVs in biomedical engineering.

Acknowledgment

Project supported by the Natural Science Foundation of Shandong Province, China (Grant Nos. ZR2022MF336 and ZR2022MD036).

References

[1] Beijersbergen M, Spreeuw R, Allen L and Woerdman J 1992 *Phys. Rev. A* **45** 1810
[2] Neuman K and Block S 2004 *Rev. Sci. Instrum.* **75** 2787
[3] Grier D 2003 *Nature* **424** 810
[4] Padgett M and Bowman R 2011 *Nat. Photon.* **5** 343
[5] Bozinovic N, Yue Y, Ren Y, Tur M, Kristensen P, Huang H, Willner A and Ramachandran S 2013 *Science* **340** 1545
[6] Wang J, Yang J, Fazal I, Ahmed N, Yan Y, Huang H, Ren Y, Yue Y, Dolinar S and Tur M 2012 *Nat. Photon.* **6** 488
[7] Ambrosio A, Marrucci L, Borbone F, Roviello A and Maddalena P 2012 *Nat. Commun.* **3** 989
[8] Toyoda K, Miyamoto K, Aoki N, Morita R and Omatsu T 2012 *Nano Lett.* **12** 3645
[9] Curtis J and Grier D 2003 *Phys. Rev. Lett.* **90** 133901
[10] Uchida M and Tonomura A 2010 *Nature* **464** 737
[11] McMorran B, Agrawal A, Anderson I, Herzing A, Lezec H, McClelland J and Unguris J 2011 *Science* **331** 192
[12] Lekner J 2007 *Phys. Rev. E* **75** 036610

[13] Pazosospina J, Franco E and Ealo J 2017 *J. Acoust. Soc. Am.* **142** 61
[14] Broadbent J and Moore D 1979 *Trans. R. Soc. Lond. A* **290** 353
[15] Hefner B and Marston P 1998 *J. Acoust. Soc. Am.* **103** 2971
[16] Gspan S, Meyer A, Bernet S and Ritsch-Marte M 2004 *J. Acous. Soc. Am.* **115** 1142
[17] Yang L, Ma Q, Tu J and Zhang D 2013 *J. Appl. Phys.* **113** 154904
[18] Zheng H, Gao L, Ma Q and Zhang D 2014 *J. Appl. Phys.* **115** 084909
[19] Gao L, Zheng H, Ma Q, Tu J and Zhang D 2014 *J. Appl. Phys.* **116** 024905
[20] Li Y, Guo G, Ma Q, Tu J and Zhang D 2017 *J. Appl. Phys.* **121** 164901
[21] Jiang X, Zhao J, Liu S, Liang B, Zou X, Yang J, Qiu C and Cheng J 2016 *Appl. Phys. Lett.* **108** 203501
[22] Courtney C, Drinkwater B, Demore C, Cochran S, Grinenko A and Wilcox P 2013 *Appl. Phys. Lett.* **102** 123508
[23] Hong Z Y, Zhang J and Drinkwater B W 2015 *Phys. Rev. Lett.* **114** 214301
[24] Courtney C, Demore C, Wu H, Grinenko A, Wilcox P, Cochran S and Drinkwater B 2014 *Appl. Phys. Lett.* **104** 154103
[25] Hong Z, Zhang J and Drinkwater B 2015 *EPL* **110** 14002
[26] Wang Q, Li Y, Ma Q, Guo G, Tu J and Zhang D 2018 *J. Appl. Phys.* **123** 034901
[27] Li P, Liu S, Peng T, Xie G, Gan X and Zhao J 2014 *Opt. Express* **22** 7598
[28] Bruus H 2012 *Lab Chip* **12** 1014